Carbon 166 (2020) 388–395

Contents lists available at ScienceDirect

Carbon

journal homepage: www.elsevier.com/locate/carbon

Defect engineering in graphene-based nanospheres enhanced hydrogen evolution reaction performance of ruthenium nanoparticles

Yongqing Shen [a, 1], Peizhi Liu [a, 1], Jinlong Du [b], Yanhui Song [a], Hailiang Cao [a], Min Zhao [a], Peng Gao [b], Bingshe Xu [a, c], Junjie Guo [a, *], Yucheng Wu [a, **]

[a] Key Laboratory of Interface Science and Engineering in Advanced Materials, Ministry of Education, Taiyuan University of Technology, Taiyuan, 030024, PR China
[b] Electron Microscopy Laboratory, School of Physics, Peking University, Beijing, 100871, PR China
[c] Materials Institute of Atomic and Molecular Science, Shaanxi University of Science & Technology, Xi'An, 710021, PR China

ARTICLE INFO

Article history:
Received 29 March 2020
Received in revised form
10 May 2020
Accepted 12 May 2020
Available online 19 May 2020

ABSTRACT

The lattice defects in graphene-based carbon materials have been proven to play a critical role for improving the hydrogen evolution reaction (HER) behavior of supported metal catalysts. Nevertheless, accurately manipulating the intensity and distribution of defects for the optimal carbon structure still remains a significant challenge. Here, the microstructures of graphene nanospheres (GNs), in the form of defects distribution and graphitization degree, are accurately regulated by annealing. The optimal electrocatalyst (Ru@GNs300) was achieved by annealing at 300 °C, giving an overpotential of 40 mV at a current density of 10 mA cm^{-2} together with superior durability in the HER performance test in 1 M KOH. Particularly, the Ru@GNs catalyst has been annealed in situ in transmission electron microscope to monitor its structural evolution. The results indicate that the aggregation of Ru nanoparticles have not been observed up to 900 °C, while the graphitization degree of carbon support increased with elevated temperature. It is worth noting that the optimized electrocatalytic activity of Ru@GNs300 originates from the annealing induced defects regulating of GNs. Thus, the structural optimizing of carbon supports by defect engineering provides an efficient approach to improve the catalytic performance for HER.

1. Introduction

Electrochemical water splitting via hydrogen evolution reaction (HER) to produce hydrogen is considered to be a sustainable and eco-friendly strategy to overcome today's worldwide energy crisis and environmental issues [1–3]. Nevertheless, the highly efficient electrocatalysts have to be adopted to trigger proton reduction with minimal overpotential and accelerate the kinetics [4,5]. Hitherto, platinum(Pt)-based catalysts enjoy "the Holy Grail" of commercial HER electrocatalysts because of their near-zero overpotential and excellent long-term durability [6–8]. Unfortunately, the exorbitant cost and limited reserves of Pt have seriously hampered their further extensive use.

Consequently, tremendous efforts have been devoted to finding suitable HER catalysts based on more economical materials such as Ru, Pd, Ni, or Mo nanoparticles and their intermetallic compounds [6,9], carbides [10,11], phosphides [12,13], sulfides [14,15], etc. Among various alternative candidates, Ru possesses a similar bond strength with hydrogen (~65 kcal mol^{-1}) together with 1/25 price of Pt metal, and thus attracts increasing scientific attention [16]. Recently, lots of groups have focused on carbon supported Ru-based electrocatalysts, such as Ru/C_3N_4/C [17], Ru/NC [16], RuCo@NC [18], Ru/C [19], Ru/GHSs [20] and Ru_xP@NPC/GHSs [21]. However, most catalysts typically suffer from the limited stability due to inevitable coalescence of metal nanoparticles during heat treatment, active site reducing and significantly catalytic activity breaking down [22–24].

Previous study on catalysts supported on carbon matrix [25–30], from defect-rich GNs to well graphitized carbon onions, indicates that the lattice defects in graphene-based carbon supports can play a role of anchoring metallic active sites, and thus improving the catalytic performance. Nevertheless, achieving the optimal carbon structure with the best defect distribution still

* Corresponding author.
** Corresponding author.
E-mail addresses: guojunjie@tyut.edu.cn (J. Guo), wyc@tyut.edu.cn (Y. Wu).
[1] Y. Shen and P. Liu contributed equally to this work.

https://doi.org/10.1016/j.carbon.2020.05.033
0008-6223/

remains great challenges. In this work, the defective GNs with tunable defects distribution and graphitization degree are accurately regulated by annealing at various temperatures, and adopted to support Ru nanoparticles towards the optimal HER electrocatalyst. Particularly, the structural evolution and anti-sintering feature of the resultant Ru@GNs composites in annealing have been monitored via in situ heating in transmission electron microscope (TEM). The results suggest that Ru@GNs annealed at 300 °C is a competitive succedaneum of Pt-based catalyst in alkaline environments with superior efficiency and long durability. This work provides a suggestive way to improve the catalytic performance by structural optimizing of carbon supports.

2. Experimental sections

2.1. Materials synthesis

The defect-rich GNs (Fig. S1) were prepared by a modified arc-discharge method in toluene, which is described in the previous paper [29]. In order to synthesis the Ru@GNs catalyst, GNs (50 mg) and $RuCl_3 \cdot 3H_2O$ (98%, MACKLIN) were dissolved in 40 mL absolute ethanol assisted with ultrasonication to prepare a mixture with Ru concentration of 15 wt%. Then the mixture was transferred into a Teflon-lined polyetheretherketone (PEEK) autoclave (100 mL) and treated with microwave irradiation in a microwave reactor (XH-8000, XiangHu Technologies, China). The autoclave was sealed and heated from room temperature (RT) to 200 °C at a heating rate of 10 °C min^{-1}, and insulated for 1 h, followed a natural cooling to RT. Continuous electromagnetic stirring was employed throughout the reaction process (temperature controlling procedure was shown as Fig. S2). After the autoclave reaction, black precipitations were obtained by centrifugation and washed with absolute ethanol for three times to remove unreacted ions, and then dried at 60 °C in a vacuum drying chamber. Finally, the catalyst was annealed under Ar at a variable temperature of 250 °C, 300 °C, 400 °C, 500 °C and 600 °C for 2 h respectively, and the products were designated as Ru@GNs250, Ru@GNs300, Ru@GNs400, Ru@GNs500, Ru@GNs600 correspondingly.

2.2. Material characterization

Scanning electron microscopy (SEM) images were taken with a dual beam system (focused ion beam and scanning electron beam, FIB-SEM, LYRA3 XMH, TESCAN, Czech), and composition identification was accomplished with EDS (X-Max^N, Oxford Instruments) equipped on the dual beam system. X-ray photoelectron spectroscopy (XPS) was performed on an X-ray Photoelectron Spectrometer (Escalab 250Xi, Thermo Fisher Scientific, USA). The charging effects were eliminated by calibrating the observed spectra with the C 1s binding energy (BE) of 284.5 eV. X-ray diffraction (XRD) studies were taken on a multipurpose X-Ray Diffractometer (Ultima IV, Rigaku, Japan. $Cu_{K\alpha}$ radiation, $\lambda = 1.5418$ Å, Rated tube voltage 40 kV and Rated tube current 40 mA). High resolution TEM was performed on a JEM2010 microscope (JEOL, Japan) under an operating voltage of 200 keV. Scanning transmission electron microscopy (STEM) images were taken using a spherical aberration (Cs) corrected low-dose STEM at 60 kV (UltraSTEM™ 200, Nion, USA). Inductively coupled plasma optical emission spectrometer (ICP-OES) was used to detect the metal content of the catalyst (720, Agilent, USA).

2.3. Electrochemical measurements

All electrochemical measurements were carried out via a standard three electrode cell system on an electrochemical workstation (CHI760E, Shanghai Chenhua Instrument Factory, China). A commercial glass carbon electrode (GCE, $\varphi = 3$ mm) served as working electrode and the counter- and the reference electrodes were a graphite rod electrode and a saturated calomel electrode (SCE), respectively. Before test, the GCE was mechanically polished with Al_2O_3 powders (0.3 μm and 0.05 μm). The working electrode were prepared as follows: 4 mg of catalyst was dispersed in the mixture of 700 μL of ethanol and 300 μL of H_2O, followed by the addition of 40 μL of 5.0 wt% Nafion (Alfa Aesar) and sonicated for 1 h to form a homogeneous ink. Then, 1.8 μL of ink was loaded on clean GCE to achieve a catalyst loading of 0.1 mg cm^{-2}. After being dried in air, the electrode was ready for testing. The potential, measured against a SCE electrode, was converted to the potential versus the reversible hydrogen electrode (vs. RHE) according to $E_{vs\ RHE} = E_{vs\ SCE} + E^0_{SCE} + 0.059 \times$ pH. Linear sweep voltammetry (LSV) with a scan rate of 2 mV s^{-1} was conducted in 1 M KOH. The Tafel slopes were obtained from the LSV curves based on the Tafel equation ($\eta = a + b \log j$, where η is overpotential, a is intercept, b is Tafel slope and j is current density). Electrochemical impedance spectroscopy (EIS) was carried out in the configuration from 10^5 to 0.01 Hz in 1 M KOH. Electrochemical double-layer capacitance (C_{dl}) measured via cyclic voltammetry (CV) were employed to evaluate the electrochemical active surface area (ECSA) in a small potential range of 0.10–0.20 V vs. RHE and scan rates of 20, 40, 60, 80, 100 mV s^{-1}. The electrolytes were purged with highly pure argon (Ar) gas for 30 min prior to measurements. All the polarization curves were collected at the steady-state and iR corrected.

2.4. In situ heating experiment

In situ heating and observation in TEM were accomplished with an in situ heating specimen holder (Lightning D9+, DENSsolutions, the Netherlands) and nano-chips (wildfire D6 Nano-Chip XT, DENSsolutions, the Netherlands) with amorphous silicon nitride support films. Samples were heated from 20 up to 1000 °C with a heating rate of 100 °C min^{-1} and incubated for 20 min at every hundreds of degrees.

3. Results and discussion

In a typical synthesis process, Ru@GNs were prepared by microwave-assisted solvothermal method without any additional reductants. The morphology and structure of the resultant Ru@GNs300 were characterized SEM, XRD, XPS and TEM, and results are shown in Fig. 1. SEM image of the catalyst and the corresponding elemental mapping of Ru and C, shown as Fig. 1a–c, demonstrate Ru is uniformly distributed on GNs. XRD measurements were applied on the as synthesized GNs, Ru@GNs and annealed Ru@GNs with different temperatures, shown as Fig. 1d and Fig. S3. In the XRD patterns, no characteristic peaks of Ru can be fitted, indicating that Ru particles may have a size of less than 4 nm and well disperse on the support [31]. The slight sharper carbon characteristic peak at 25.9° of Ru@GNs300 indicates the decrease of defects, and thus the increase of graphitization degree after annealing. XPS survey spectrum of Ru@GNs300 shows distinct signals of Ru, C and O (Fig. 1e and Fig. S4). From the high resolution XPS scan, binding energies of Ru $3p_{3/2}$ and Ru $3p_{1/2}$ were determined as 462.3 and 484.7 eV respectively (Fig. 1e), and Ru $3d_{3/2}$ and Ru $3d_{5/2}$ were observed at 284.4 and 280.6 eV respectively (Fig. S4b), verifying the presence of zero valence Ru (Ru^0) in the resultant nanocrystals [31,32]. TEM image (Fig. 1f) of Ru@GNs300 shows a homogeneous dispersion of Ru nanoparticles with particle size distribution (PSD) of (1.99 ± 0.46) nm on the GNs support. The magnified image (Fig. 1g) shows that Ru nanocrystals disperse on GNs composed of ripple-rich graphitic layers. The previous report

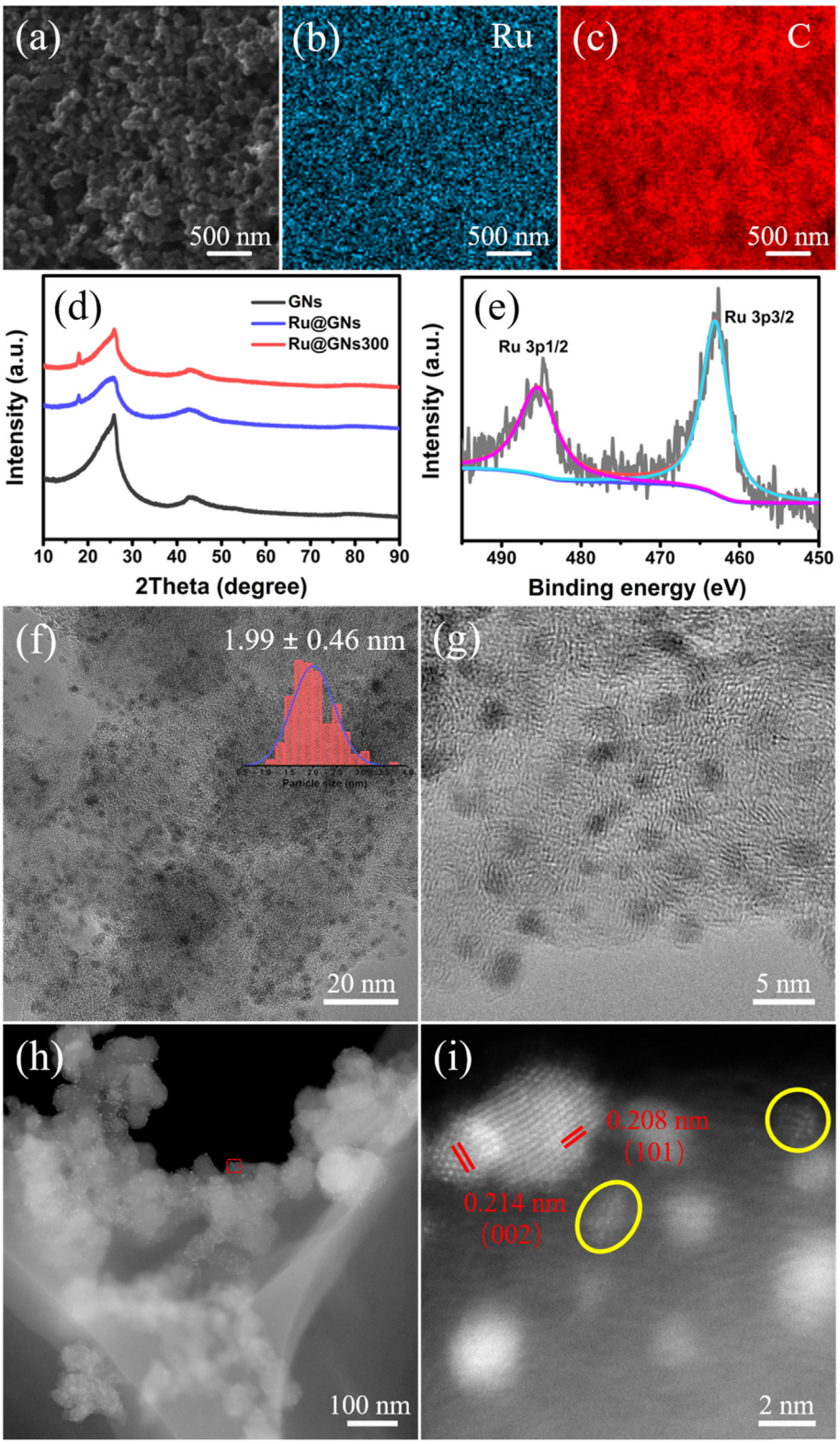

Fig. 1. The structural characterization of Ru@GNs300. (a) SEM image of Ru@GNs300. (b, c) Energy dispersive spectrometry (EDS) mapping of Ru and C corresponding to (a). (d) XRD patterns of GNs, Ru@GNs, and Ru@GNs300, respectively. (e) High resolution XPS spectrum of Ru@GNs300, with a resolving of Ru $3p_{1/2}$ and $3p_{3/2}$ state. (f) TEM image of Ru@GNs300, and particle size distribution of Ru in the catalyst is shown as the inset. (g) The magnified TEM image. (h) HAADF image of Ru@GNs300, and (i) is a zooming in of the dashed box in (h). (A colour version of this figure can be viewed online.)

suggests that the lattice defects can induce the ripples in the graphene layers and provides effective anchoring sites for the Ru nanocrystals [33]. In other words, the configuration of defect-rich GNs can effectively prevent the aggregation of Ru particles, which is advantageous to the electrocatalytic activity.

To further characterize the microstructure of the catalyst, Cs-corrected STEM with high angle annular dark field (HAADF) imaging was employed. Fig. 1h is an overview HAADF image of the Ru@GNs catalyst, in which the image intensity is roughly proportional to Z^2 (Z is the atomic number of a certain element). Thus, HAADF image contrast of metal particles and carbon in the catalyst is determined by the atomic number Z, and is generally unaffected by small changes in defocus and specimen thickness [34–36]. It is clearly identified that enormous amount of Ru particles (bright dots in the image) disperse uniformly in GNs (spheres with less brightness), which is consisted with the result of Fig. 1f and g. Fig. 1i is a zooming in image of the thin corner enclosed by the dashed box in Fig. 1h. Atomic arrangements of nanoparticles on the top left corner were clearly resolved, and the lattice fringe with spacing of 0.208 and 0.214 nm could be assigned to the (101) and (002) crystal planes of Ru^0 crystal ($P6_3/mmc$ (194), PDF#88–1734), respectively, which have a better HER activity according to the density functional theory (DFT) calculations [37]. Nanocrystals in the yellow circle are slightly defocused, and other grains are out of focus. Compared with TEM imaging, Cs-corrected HAADF image has a much shorter focal depth of only a few nanometers [38], from which the burial depth of nanoparticles in support can be resolved. The asynchronous focus of Ru nanocrystals demonstrates that Ru nanoparticles disperse uniformly on the graphitic layers of GNs in three dimensions.

N_2 absorption-desorption isotherms were also employed to characterize the BET surface area and pore size distribution of the surface-modified Ru@GNs300. As can be seen in Fig. S5, a type-II isotherm with a H3-type hysteresis loop [18] is obtained, displaying a specific surface area of 109 $m^2\ g^{-1}$, which may arise from the edge defects of carbon material interfering with the stacking of graphene sheets [39]. The pore size distribution (insert image) revealed a strong and narrow distribution centered at ~3 nm. The result is consisted with the PSD of Ru nanoparticles measured by STEM, and the large specific surface of GNs support and small size distribution of Ru nanocrystals are beneficial to the catalytic properties.

The HER performance of as synthesized catalyst (Ru@GNs) and catalysts annealed in Ar atmosphere at a series of temperature were measured, with GNs support and 20% commercial Pt/C catalyst concurrently as control groups, and the results are shown as Fig. 2a and Fig. S6. GNs support scarcely shows any catalytic activity, and all the Ru decorated catalysts exhibit excellent activities comparable to commercial Pt/C catalyst. Especially Ru@GNs300 exhibits a onset potential of ~0 mV vs. RHE and achieves a current density of 10 mA cm^{-2} at an overpotential of 40 mV, which is lower than that of the Pt/C catalyst (60 mV), as well as other recently reported HER

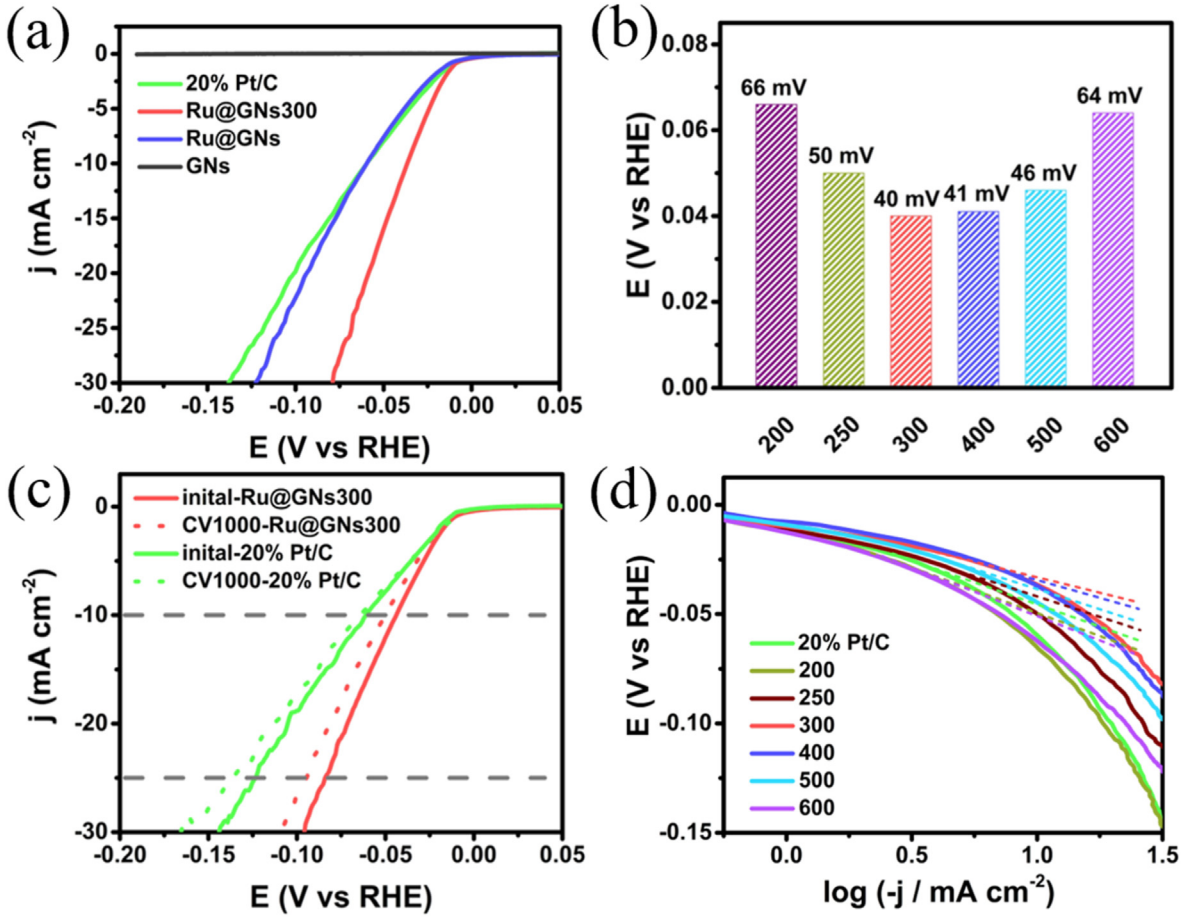

Fig. 2. Electrocatalytic HER performance tests of catalysts in 1 M KOH solution. (a) HER polarization curves of 20% commercial Pt/C, GNs, Ru@GNs and Ru@GNs300 at a scan rate of 2 mV s^{-1}. (b) Volcano plots of overpotential of catalyst annealed at various temperatures measured at a current density of 10 mA cm^{-2}. (c) HER polarization curves of 1.90 wt% Ru@GNs300 and Pt/C electrocatalyst at initial state and after 1000 cycles. (d) Tafel slopes of these catalysts with different annealing temperature. (A colour version of this figure can be viewed online.)

electrocatalysts [13,40–42], and the detailed comparison are listed in Table S1. Fig. 2b is the volcano plot of overpotential of these annealed catalysts measured at a current density of 10 mA cm^{-2}. It confirms that Ru@GNs300 possesses the best electrocatalytic activity.

The stability of Ru@GNs300 under alkaline conditions was tested by CV techniques and chronoamperometry measurements. As illustrated in Fig. 2c, the polarization curves of Ru@GNs300 after 1000 cycles keep almost the same as the initial test, and the overpotential increased by 6 mV at the current density of 10 mA cm^{-2}, which is still much superior to the initial state of Pt/C. In Fig. S7, at a constant overpotential of 40 mV, Ru@GNs300 showed an excellent HER stability with the current density decreased in magnitude only slightly over 24 h of continuous operation. What is more, the structure of Ru@GNs300 were preserved after 1000 cycles and the PSD of the Ru nanoparticles (Fig. S8) was almost the same as that in the fresh catalyst, indicating an excellent structural stability. Note that the loading amount of Ru in Ru@GNs300 for the catalytic measurement is as low as 1.90 wt%, as determined by an ICP-OES measurement, hence enable it a cheaper alternative to Pt-based electrocatalysts in HER applications under alkaline media. Additionally, Ru@GNs300 has a small Tafel slope of 28 mV $decade^{-1}$, shown as Fig. 2d, which is smaller than that of Pt/C (39 mV $decade^{-1}$), implying the rapid electron transfer process [43]. The Nyquist plots demonstrate that the diameter of the semicircle for Ru@GNs300 in the high-frequency region was smaller compared to those of the other catalysts (Fig. S9), indicating that Ru@GNs300 possesses a faster charge transfer capacity during the HER process [44]. We attribute the efficiency to a synergic effect between the Ru nanoparticles and the GNs that help reduce the charge transfer resistance at the catalyst/electrolyte interface, thus increasing the electrochemical conductivity [33,45]. In addition, the results in Fig. S10 suggest that the C_{dl} value, equivalent to the ECSA of the catalyst, increase to the maximum at 300 °C and slightly decreased with an further increasing annealing temperature, which is consistent with the electrocatalytic activity trend and indicates that the Ru@GNs300 sample possessed the largest active surface area. The ECSA of Ru@GNs300 is 4.75 cm^2, which is almost equal to that of Pt/C (4.45 cm^2, calculation details are described in Fig. S10), indicating that the intrinsic HER catalysis of Ru@GNs300 is superior to Pt/C. Based on the above electrochemical results, the favorable HER kinetics and abundant density of active sites account for the outstanding activity of the Ru@GNs300 catalyst.

To further explore the electrocatalysis mechanism of the catalyst, structure evolutions of Ru@GNs were studied with in situ heating experiment in TEM. With the increase of the annealing temperature, the mean particle size of Ru nanoparticles on GNs only exhibit a slight increase from 1.99 nm (at 300 °C, shown as Fig. 1f) to 2.24 nm (at 600 °C, shown as Fig. S11), and the dispersion of Ru nanoparticles stayed uniform similarly. The in situ heating in TEM was performed from 20 to 1000 °C, and the results are shown as Fig. 3. During in situ heating, Ru nanoparticles did not exhibit a morphological change, and the PSD histograms (Fig. S12) show that size of Ru nanoparticles slightly increases form 1.91 nm at 20 °C to 2.30 nm at 1000 °C, which is consistent with the XRD and ex situ annealing results discussed previously. However, the

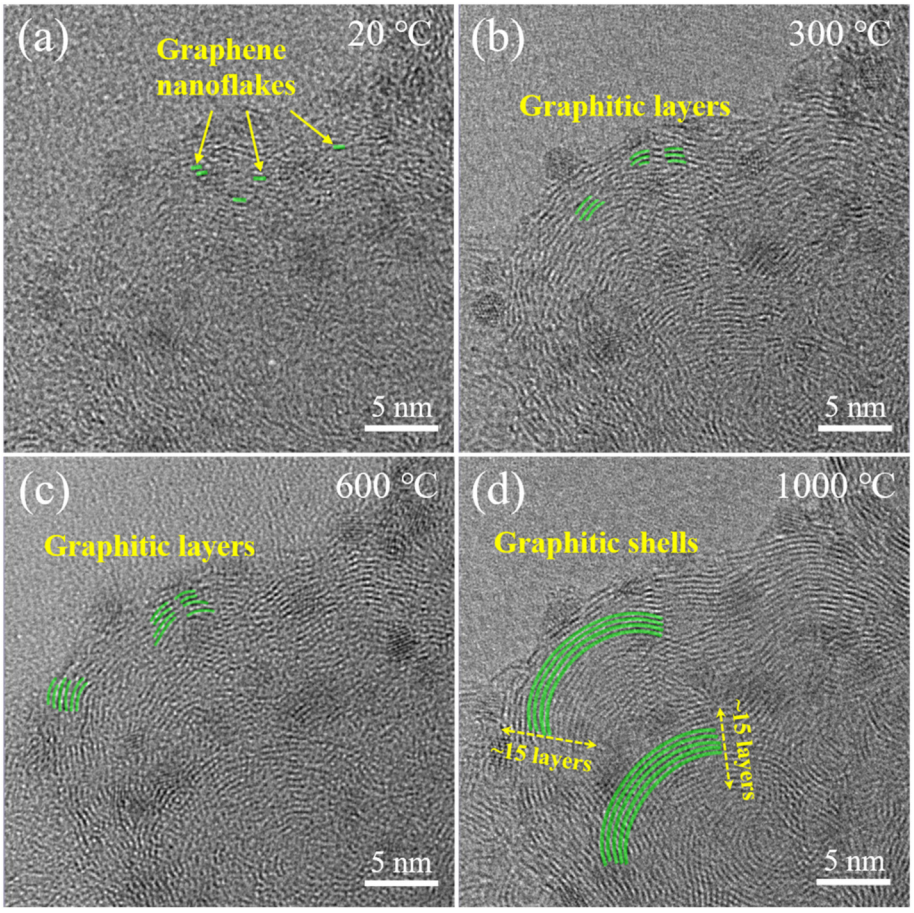

Fig. 3. High resolution TEM images of Ru@GNs. (a–d) catalysts at temperatures of 20, 300, 600 and 1000 °C, respectively. Green sketches are used to illustrate the graphitic layers. (A colour version of this figure can be viewed online.)

microstructure of GNs changes significantly. From Fig. 3a–d, the growth of graphene nanoflakes to onion-like graphitic shells can be clearly observed with the continuously increased temperature [46]. Originally, GNs are composed of mono-layer graphene nanoflakes at 20 °C (Fig. 3a). The length and stacking number of (002) graphitic layers with an interplanar spacing of 0.34 nm increased visibly from 300 °C (Fig. 3b) to 600 °C (Fig. 3c). In the end, onion-like graphitic shells of ~15 layers formed at 1000 °C (Fig. 3d). The consistent result can be confirmed by selected area diffraction patterns of the catalyst shown in Fig. S12, in which the diffused rings (Fig. S12a) of carbon became sharp (Fig. S12d) after a high temperature heating. The increase of graphitization degree indicates a decrease of the defects in curved graphitic layers and thus a decrease in the sites of anchoring Ru nanoparticles, which explains the electrocatalytic activity degradation of Ru@GNs beyond annealing temperature of 300 °C.

To confirm the electrocatalysis mechanism of the catalyst, in situ analyses were also performed on 20% commercial Pt/C, and the results are shown in Fig. 4. As shown in Fig. 4a–c, the Ru nanoparticles do not undergo significant migration and coalescence till 1000 °C, and only a few Ru particles, highlighted with purple circles, showed apparently aggregation after 900 °C. Other particles do not migrate together during the entire heating process. Combined with the PSD statistics mentioned in Fig. S12, the growth of the particles before 900 °C is dominated by the Ostwald ripening sintering mechanism [47]. In sharp contrast, the Pt nanoparticles in Pt/C aggregated extensively from 200 °C and the morphology of the catalyst changed completely, shown as Fig. 4d–f. When the temperature rose to 600 °C, particle migration and coalescence became more rapid and the sintering behavior of Pt nanoparticles is shown in Fig. S13. These results demonstrate that the high-defect GNs could serve as an effective barrier to prevent the migration of Ru nanoparticles during calcination, since the Ru nanoparticles can be anchored by the defects of the GNs to become sinter-resistant.

The comprehensive structure-activity relationship study on Ru@GNs gives a clear clue of its electrocatalysis mechanism. GNs support scarcely shows any HER catalytic activity, while Ru decorated catalysts exhibit excellent activities comparable to the activity of commercial Pt/C. This indicates that the activity originates from the interaction between Ru nanoparticles and defects in GNs support, which is consistent with the DFT calculations on the similar system such as coupled molybdenum carbide and pyridinic N doped reduced graphene oxide [48], and cobalt encapsulated by N,B doped carbon cages [49]. A well disperse of Ru nanoparticles in GNs, and the increasing of annealing temperature does not cause an observable aggregation of Ru nanoparticles and a significant reduce of the electrochemical activity. This demonstrates the defective structure of GNs play a critical role in stabilizing Ru nanoparticles and enhancing the electrocatalytic behavior. The well controlled annealing is proven to be an effective way to accurately regulate the intensity and distribution of defects of carbon matrix, and thus improve the supported metal catalyst. However, the activity of an overaged catalyst is hindered because of the complete graphitization of carbon support. Therefore, Ru@GNs300 guarantees a good stability and a large number of catalytically active sites, which explain its optimal electrochemical hydrogen evolution performance.

4. Conclusions

In summary, a highly active and stable electrocatalytic system based on GNs-supported Ru nanoparticles was achieved with superior HER performance in alkaline media. Ru@GNs300 possessed the optimized electrocatalytic activity of a 0 mV onset overpotential, a 40 mV overpotential at 10 mA cm^{-2}, a small Tafel slope

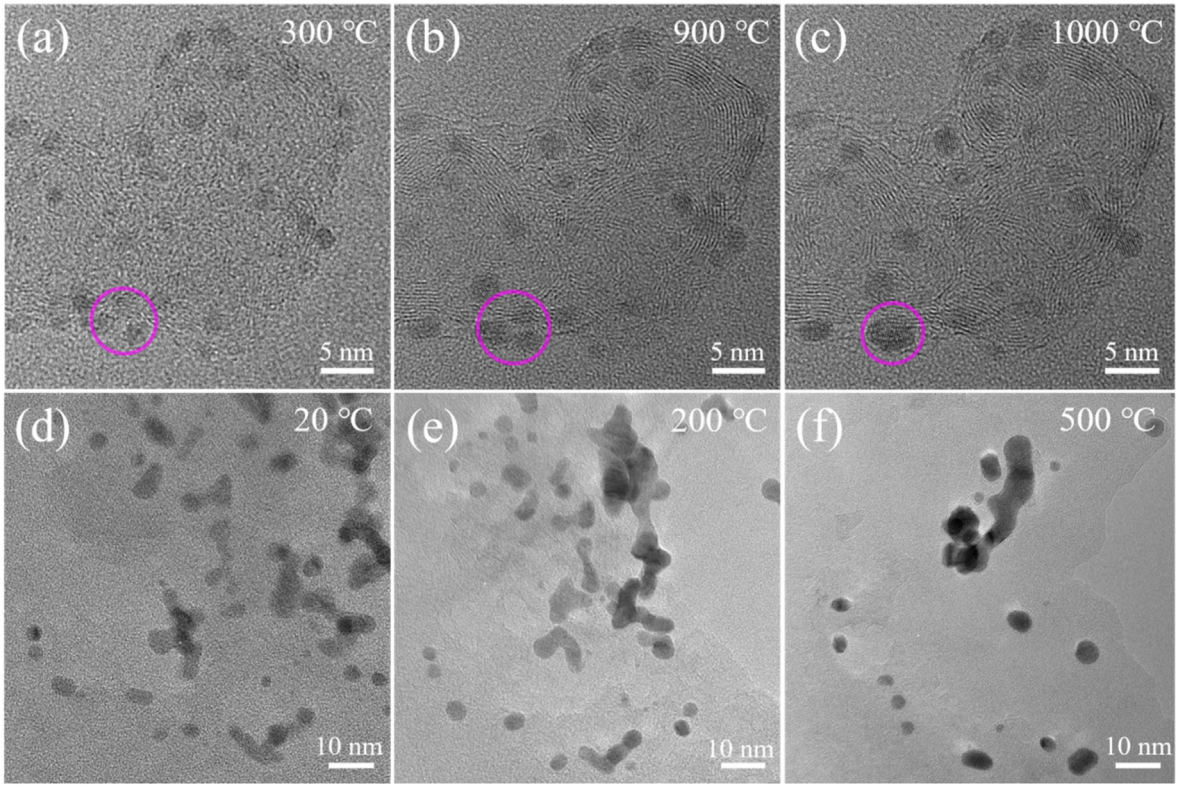

Fig. 4. Comparison of thermal stability between Ru@GNs and 20% commercial Pt/C catalysts. (a–c) Ru@GNs and (d–f) Pt/C at different calcination temperatures in TEM. (A colour version of this figure can be viewed online.)

and excellent durability, which is comparable/superior to results reported in recent literatures and 20% commercial Pt/C. PSD of Ru in the catalyst is ~2 nm and Ru loading is 1.90 wt%, which provide a huge economical advantage in price over Pt/C catalysts. More excitingly, the Ru@GNs delivered a robust thermal stability from 20 to 1000 °C, which provides the possibility for the electrolysis of water in an industrial setting. The thorough and comprehensive structure-activity relationship study indicates that the large specific surface area, superior conductivity, high active site density of the GNs support enhance the stability and dispersion of Ru nanoparticles, and the interaction between Ru nanoparticles and GNs support contribute to the superior activity of the catalyst.

Declaration of competing interest

The authors declare that they have no known competing financial interests or personal relationships that could have appeared to influence the work reported in this paper.

CRediT authorship contribution statement

Yongqing Shen: Writing - original draft. **Peizhi Liu:** Writing - original draft. **Jinlong Du:** Writing - original draft. **Yanhui Song:** Writing - original draft. **Hailiang Cao:** Writing - original draft. **Min Zhao:** Writing - original draft. **Peng Gao:** Writing - original draft. **Bingshe Xu:** Supervision, Writing - original draft. **Junjie Guo:** Supervision, Writing - original draft. **Yucheng Wu:** Supervision, Writing - original draft.

Acknowledgements

This research has been supported by National Natural Science Foundation of China (51501124, 51602212, and U1810204), Natural Science Foundation of Shanxi Province (201701D221073, 201901D111107, 201901D211046), Scientific and Technological Innovation Programs of Higher Education Institutions in Shanxi (STIP, 2019L0120, 2019L0253, 2019L0346), and Program for the Innovative Talents of Higher Education Institutions in Shanxi, Special Foundation for Youth SanJin Scholars.

Appendix A. Supplementary data

Supplementary data to this article can be found online at https://doi.org/10.1016/j.carbon.2020.05.033.

References

[1] L. Chen, X.L. Dong, Y.G. Wang, Y.Y. Xia, Separating hydrogen and oxygen evolution in alkaline water electrolysis using nickel hydroxide, Nat. Commun. 7 (2016) 11741.
[2] L.C. Seitz, C.F. Dickens, K. Nishio, Y. Hikita, J. Montoya, A. Doyle, et al., A highly active and stable $IrO_x/SrIrO_3$ catalyst for the oxygen evolution reaction, Science 353 (2016) 1011–1014.
[3] Y. Zheng, Y. Jiao, M. Jaroniec, S.Z. Qiao, Advancing the electrochemistry of the hydrogen-evolution reaction through combining experiment and theory, Angew. Chem. Int. Ed. 54 (2015) 52–65.
[4] H. Li, H.X. Zhang, X.L. Yan, B.S. Xu, J.J. Guo, Carbon-supported metal single atom catalysts, N. Carbon Mater. 33 (2018) 1–11.
[5] M.X. Song, Y.H. Song, W.B. Sha, B.S. Xu, J.J. Guo, Y.C. Wu, Recent advances in non-precious transition metal/nitrogen-doped carbon for oxygen reduction electrocatalysts in PEMFCs, Catalysts 10 (2020) 141.
[6] S. Bai, C.M. Wang, M.S. Deng, M. Gong, Y. Bai, J. Jiang, et al., Surface polarization matters: enhancing the hydrogen-evolution reaction by shrinking Pt shells in Pt-Pd-graphene stack structures, Angew. Chem. Int. Ed. 53 (2014) 12120–12124.
[7] C.-D. Si, Z.-X. Wu, J. Wang, Z.-H. Lu, X.-F. Xu, J.-S. Li, Enhanced the hydrogen evolution performance by ruthenium nanoparticles doped into cobalt phosphide nanocages, ACS Sustain. Chem. Eng. 7 (2019) 9737–9742.
[8] H.M. Sun, X.B. Xu, Z.H. Yan, X. Chen, F.Y. Cheng, P.S. Weiss, et al., Porous multishelled Ni_2P hollow microspheres as an active electrocatalyst for hydrogen and oxygen evolution, Chem. Mater. 29 (2017) 8539–8547.
[9] J.T. Chen, G.L. Xia, P. Jiang, Y. Yang, R. Li, R.H. Shi, et al., Active and durable hydrogen evolution reaction catalyst derived from Pd-doped metal–organic frameworks, ACS Appl. Mater. Interfaces 8 (2016) 13378–13383.
[10] L. Liao, S.N. Wang, J.J. Xiao, X.J. Bian, Y.H. Zhang, M.D. Scanlon, et al., A nanoporous molybdenum carbide nanowire as an electrocatalyst for hydrogen evolution reaction, Energy Environ. Sci. 7 (2014) 387–392.
[11] Y. Yan, B.Y. Xia, X.Y. Qi, H.B. Wang, R. Xu, J.Y. Wang, et al., Nano-tungsten carbide decorated graphene as co-catalysts for enhanced hydrogen evolution on molybdenum disulfide, Chem. Commun. 49 (2013) 4884–4886.
[12] J.-S. Li, S. Zhang, J.Q. Sha, H. Wang, M.Z. Liu, L.X. Kong, et al., Confined molybdenum phosphide in P-doped porous carbon as efficient electrocatalysts for hydrogen evolution, ACS Appl. Mater. Interfaces 10 (2018) 17140–17146.
[13] Z. Pu, I.S. Amiinu, Z. Kou, W. Li, S. Mu, RuP_2-based catalysts with platinum-like activity and higher durability for the hydrogen evolution reaction at all pH values, Angew. Chem. Int. Ed. 56 (2017) 11559–11564.
[14] J. Staszak-Jirkovsky, C.D. Malliakas, P.P. Lopes, N. Danilovic, S.S. Kota, K.C. Chang, et al., Design of active and stable Co-Mo-S_x chalcogels as pH-universal catalysts for the hydrogen evolution reaction, Nat. Mater. 15 (2016) 197–203.
[15] D. Voiry, M. Salehi, R. Silva, T. Fujita, M. Chen, T. Asefa, et al., Conducting MoS_2 nanosheets as catalysts for hydrogen evolution reaction, Nano Lett. 13 (2013) 6222–6227.
[16] J. Zhang, P. Liu, G. Wang, P.P. Zhang, X.D. Zhuang, M.W. Chen, et al., Ruthenium/nitrogen-doped carbon as an electrocatalyst for efficient hydrogen evolution in alkaline solution, J. Mater. Chem. A 5 (2017) 25314–25318.
[17] Y. Zheng, Y. Jiao, Y.H. Zhu, L.H. Li, Y. Han, Y. Chen, et al., High electrocatalytic hydrogen evolution activity of an anomalous ruthenium catalyst, J. Am. Chem. Soc. 138 (2016) 16174–16181.
[18] J.W. Su, Y. Yang, G.L. Xia, J.T. Chen, P. Jiang, Q.W. Chen, Ruthenium-cobalt nanoalloys encapsulated in nitrogen-doped graphene as active electrocatalysts for producing hydrogen in alkaline media, Nat. Commun. 8 (2017) 14969.
[19] J. Ohyama, T. Sato, Y. Yamamoto, S. Arai, A. Satsuma, Size specifically high activity of Ru nanoparticles for hydrogen oxidation reaction in alkaline electrolyte, J. Am. Chem. Soc. 135 (2013) 8016–8021.
[20] J.-S. Li, M.-J. Huang, L.-X. Kong, X.-N. Chen, Y.-W. Zhou, J.-L. Li, et al., Ruthenium nanoparticles anchored on graphene hollow nanospheres superior to platinum for the hydrogen evolution reaction in alkaline media, Inorg. Chem. 59 (2020) 930–936.
[21] J.-S. Li, J.-Y. Li, M.-J. Huang, L.-X. Kong, Z.X. Wu, Anchoring Ru_xP on 3D hollow graphene nanospheres as efficient and pH-universal electrocatalysts for the hydrogen evolution reaction, Carbon 161 (2020) 44–50.
[22] C.T. Campbell, The energetics of supported metal nanoparticles: relationships to sintering rates and catalytic activity, Accounts Chem. Res. 46 (2013) 1712–1719.
[23] A.K. Datye, Q. Xu, K.C. Kharas, J.M. Mccarty, Particle size distributions in heterogeneous catalysts: what do they tell us about the sintering mechanism? Catal. Today 111 (2006) 59–67.
[24] T.W. Hansen, A.T. Delariva, S.R. Challa, A.K. Datye, Sintering of catalytic nanoparticles: particle migration or Ostwald ripening? Accounts Chem. Res. 46 (2013) 1720–1730.
[25] J.J. Guo, X.M. Wang, B.S. Xu, One-step synthesis of carbon-onion-supported platinum nanoparticles by arc discharge in an aqueous solution, Mater. Chem. Phys. 113 (2009) 179–182.
[26] M.X. Song, Y.H. Song, H. Li, P.Z. Liu, B.S. Xu, H. Wei, et al., Sucrose leavening-induced hierarchically porous carbon enhanced the hydrogen evolution reaction performance of Pt nanoparticles, Electrochim. Acta 320 (2019) 134603.
[27] B.S. Xu, J.J. Guo, X.M. Wang, X.G. Liu, H. Ichinose, Synthesis of carbon nanocapsules containing Fe, Ni or Co by arc discharge in aqueous solution, Carbon 44 (2006) 2631–2634.
[28] X.L. Yan, P. Duan, F.W. Zhang, H. Li, H.X. Zhang, M. Zhao, et al., Stable single-atom platinum catalyst trapped in carbon onion graphitic shells for improved chemoselective hydrogenation of nitroarenes, Carbon 143 (2019) 378–384.
[29] X.L. Yan, H. Li, J.T. Sun, P.Z. Liu, H.X. Zhang, B.S. Xu, et al., Pt nanoparticles decorated high-defective graphene nanospheres as highly efficient catalysts for the hydrogen evolution reaction, Carbon 137 (2018) 405–410.
[30] X.F. Zhang, J.J. Guo, P.F. Guan, C.J. Liu, H. Huang, F.H. Xue, et al., Catalytically active single-atom niobium in graphitic layers, Nat. Commun. 4 (2013) 1924.
[31] J. Wang, Z.Z. Wei, S.J. Mao, H.R. Li, Y. Wang, Highly uniform Ru nanoparticles over N-doped carbon: pH and temperature-universal hydrogen release from water reduction, Energy Environ. Sci. 11 (2018) 800–806.
[32] M. Zhao, Z.T. Chen, Z.H. Lyu, Z.D. Hood, M.H. Xie, M. Vara, et al., Ru octahedral nanocrystals with a face-centered cubic structure, {111} facets, thermal stability up to 400 °C, and enhanced catalytic activity, J. Am. Chem. Soc. 141 (2019) 7028–7036.
[33] J.J. Guo, Z. Mao, X.L. Yan, R. Su, P.F. Guan, B.S. Xu, et al., Ultrasmall tungsten carbide catalysts stabilized in graphitic layers for high-performance oxygen reduction reaction, Nano Energy 28 (2016) 261–268.
[34] P.Z. Liu, H.F. Tian, W. Windl, G. Gu, G. Duscher, Y.C. Wu, et al., Direct imaging of the nitrogen-rich edge in monolayer hexagonal boron nitride and its band structure tuning, Nanoscale 11 (2019) 20676–20684.
[35] D.B. Williams, C.B. Carter, The Transmission Electron Microscope: a Text Book for Materials Science, second ed., Springer US, 2009, pp. p379–p381 (chapter 22).4 Z-contrast.

[36] H.X. Zhang, W.W. Liu, Z.H. Zhang, M.F. Li, B.S. Xu, J.J. Guo, Direct imaging of a single Ni atom cutting graphene to form a graphene nanomesh, Phys. Chem. Chem. Phys. 20 (2018) 26814–26818.
[37] Y.T. Li, L.A. Zhang, Y. Qin, F.Q. Chu, Y. Kong, Y.X. Tao, et al., Crystallinity dependence of ruthenium nanocatalyst toward hydrogen evolution reaction, ACS Catal. 8 (2018) 5714–5720.
[38] P.Z. Liu, G.L. Li, G. Duscher, Y.K. Sharma, A.C. Ahyi, T. Isaacs-Smith, et al., Roughness of the SiC/SiO_2 vicinal interface and atomic structure of the transition layers, J. Vac. Sci. Technol. A 32 (2014), 060603.
[39] J.J. Guo, J.R. Morris, Y. Ihm, C.I. Contescu, N.C. Gallego, G. Duscher, et al., Topological defects: origin of nanopores and enhanced adsorption performance in nanoporous carbon, Small 8 (2012) 3283–3288.
[40] P. Jiang, J.T. Chen, C.L. Wang, K. Yang, S.P. Gong, S. Liu, et al., Tuning the activity of carbon for electrocatalytic hydrogen evolution via an iridium-cobalt alloy core encapsulated in nitrogen-doped carbon cages, Adv. Mater. 30 (2018) 1705324.
[41] P.T. Wang, X. Zhang, J. Zhang, S. Wan, S.J. Guo, G. Lu, et al., Precise tuning in platinum-nickel/nickel sulfide interface nanowires for synergistic hydrogen evolution catalysis, Nat. Commun. 8 (2017) 14580.
[42] G. Zhang, G.C. Wang, Y. Liu, H.J. Liu, J.H. Qu, J.H. Li, Highly active and stable catalysts of phytic acid-derivative transition metal phosphides for full water splitting, J. Am. Chem. Soc. 138 (2016) 14686–14693.
[43] J.-S. Li, J.-Y. Li, X.-R. Wang, S. Zhang, J.-Q. Sha, G.-D. Liu, Reduced graphene oxide-supported MoP@P-doped porous carbon nano-octahedrons as high-performance electrocatalysts for hydrogen evolution, ACS Sustain. Chem. Eng. 6 (2018) 10252–10259.
[44] J.-S. Li, L.-X. Kong, Z.-X. Wu, S. Zhang, X.-Y. Yang, J.-Q. Sha, et al., Polydopamine-assisted construction of cobalt phosphide encapsulated in N-doped carbon porous polyhedrons for enhanced overall water splitting, Carbon 145 (2019) 694–700.
[45] W.D. Li, Y. Liu, M. Wu, X.L. Feng, S.a.T. Redfern, Y. Shang, et al., Carbon-quantum-dots-loaded ruthenium nanoparticles as an efficient electrocatalyst for hydrogen production in alkaline media, Adv. Mater. 30 (2018) 1800676.
[46] M.F. Li, W.W. Liu, H.X. Zhang, Z.L. Liang, P. Duan, X.L. Yan, et al., Direct imaging of construction of carbon onions by curling few-layer graphene flakes, Phys. Chem. Chem. Phys. 20 (2018) 2022–2027.
[47] S.R. Challa, A.T. Delariva, T.W. Hansen, S. Helveg, J. Sehested, P.L. Hansen, et al., Relating rates of catalyst sintering to the disappearance of individual nanoparticles during Ostwald ripening, J. Am. Chem. Soc. 133 (2011) 20672–20675.
[48] J.-S. Li, Y. Wang, C.-H. Liu, S.-L. Li, Y.-G. Wang, L.-Z. Dong, et al., Coupled molybdenum carbide and reduced graphene oxide electrocatalysts for efficient hydrogen evolution, Nat. Commun. 7 (2016) 11204.
[49] H.B. Zhang, Z.J. Ma, J.J. Duan, H.M. Liu, G.G. Liu, T. Wang, et al., Active sites implanted carbon cages in core-shell architecture: highly active and durable electrocatalyst for hydrogen evolution reaction, ACS Nano 10 (2016) 684–694.